

Giant cavities, cooling and metallicity substructure in Abell 2204

J. S. Sanders^{1*}, A. C. Fabian¹ and G. B. Taylor²

¹ *Institute of Astronomy, Madingley Road, Cambridge. CB3 0HA*

² *Department of Physics and Astronomy, University of New Mexico, Albuquerque, NM 87131. USA*

29 October 2018

ABSTRACT

We present results from deep *Chandra* and *XMM-Newton* observations of the relaxed X-ray luminous galaxy cluster Abell 2204. We detect metallicity inhomogeneities in the intracluster medium on a variety of distance scales, from a ~ 12 kpc enhancement containing a few times $10^7 M_{\odot}$ of iron in the centre, to a region at 400 kpc radius with an excess of a few times $10^9 M_{\odot}$. Subtracting an average surface brightness profile from the X-ray image yields two surface brightness depressions to the north and south of the cluster. Their morphology is similar to the cavities observed in cluster cores, but they have radii of 240 kpc and 160 kpc and have a total enthalpy of 2×10^{62} erg. If they are fossil radio bubbles, their buoyancy timescales imply a total mechanical heating power of 5×10^{46} erg s^{-1} , the largest such bubble heating power known. More likely, they result from the accumulation of many past bubbles. Energetically this is more feasible, as the enthalpy of these regions could combat X-ray cooling in this cluster to 500 kpc radius for around 2 Gyr. The core of the cluster also contains five to seven ~ 4 kpc radius surface brightness depressions that are not associated with the observed radio emission. If they are bubbles generated by the nucleus, they are too small to balance cooling in the core by an order of magnitude. However if the radio axis is close to the line of sight, projection effects may mask more normal bubbles. Using RGS spectra we detect a Fe XVII line. Spectral fitting reveals temperatures down to ~ 0.7 keV; the cluster therefore shows a range in X-ray temperature of at least a factor of 15. The quantity of low temperature gas is consistent with a mass deposition rate of $65 M_{\odot} \text{ yr}^{-1}$.

Key words: X-rays: galaxies — galaxies: clusters: individual: Abell 2204 — intergalactic medium — cooling flows

1 INTRODUCTION

Abell 2204 is a luminous galaxy cluster at a redshift of 0.1523 ($L_X = 2 \times 10^{45} h_{50}^{-2}$ erg s^{-1} in the 2–10 keV band; Edge et al. 1990). On large scales the cluster has a regular morphology (Buote & Tsai 1996; Schuecker et al. 2001; Hashimoto et al. 2007), appearing relaxed. Reiprich et al. (2008) recently used a *Suzaku* observation of this cluster to measure its temperature near to the virial radius, finding it close to predictions from hydrodynamic simulations.

We previously analysed a short snapshot observation of the cluster by *Chandra* (Sanders et al. 2005). The core of the cluster has a fairly complex structure, containing a flat plateau and plume-like feature. One of the most peculiar features was a high-metallicity ring found around the core of the cluster, which we hypothesised may have been due to a merger in the past.

Here we present results from a deep 77 ks *Chandra* observations of this cluster, in addition to new VLA radio observations. We assume $H_0 = 70 \text{ km s}^{-1} \text{ Mpc}^{-1}$ and $\Omega_{\Lambda} = 0.7$, translating to a scale of 2.6 kpc per arcsec. Metallicity measurements assume the relative

Table 1. *Chandra* observations analysed in this paper.

Observation ID	Detector	Observation date	Exposure (ks)
499	ACIS-S	2000-07-29	10.1
6104	ACIS-I	2004-09-20	9.6
7940	ACIS-I	2007-06-06	77.1

Solar abundances of Anders & Grevesse (1989). Abell 2204 has a weighted Galactic hydrogen column density of $5.7 \times 10^{20} \text{ cm}^{-2}$ determined by HI surveys (Kalberla et al. 2005).

2 DATA PROCESSING

The data analysed in this paper come from three different observations of the cluster by *Chandra* (Table 1). Two of the observations were taken in the ACIS-I detector mode, which uses lower detector background front-illuminated CCDs. The other observation was made which with the ACIS-S detector mode, which has a higher background, but larger effective area, smaller field of view, and better energy resolution.

* E-mail: jss@ast.cam.ac.uk

For the part of the analysis concentrated in the bright central region, we use all three datasets in combination. In the outer region we concentrate on the 7940 and 6104 datasets, or just the 7940 dataset, as they have a lower non-X-ray background.

Each of the observations was made with the ACIS VFAINT mode. We applied this VFAINT filtering to reduce the detector background, after ensuring the observations used the latest gain files.

2.1 Background modelling

Comparison of spectra extracted from the edge of the ACIS-I observations compared to standard blank-sky observations showed excess soft emission. This soft emission appears to be spatially flat, not declining with radius from the cluster centre, indicating it is not cluster emission and likely Galactic in origin. The emission is very similar between the 6104 and 7940 observations, showing it is not a time-variable background.

Rather than use standard blank-sky observations, we decided to construct our own backgrounds to account for this soft emission. Firstly we took stowed background observations (where the detector is not observing the sky). These observations, after normalising to the observations in the 9–12 keV band and removing VFAINT-filtered events, closely match the particle and detector backgrounds.

To account for the Galactic and extragalactic X-ray emission, we modelled a far off axis region (after accounting for the particle background) with a thermal model (fixed at a temperature of 0.25 keV and Solar metallicity) plus powerlaw ($\Gamma = 1.5$) model. This model was a good fit to the data ($\chi^2_{\nu} = 211/225 = 0.94$). Taking this model, we simulated spectra in a grid over the detector (iterating in 8×8 detector pixel cells) for each of the observations, taking into account the change in effective area by using ancillary response files generated at each grid point. By deconstructing the spectra into individual events (randomising spatially within each grid point), we generated simulated events files for each observation. This X-ray background event file was then merged with the normalised stowed background event file to make a total background event file (we simulated the X-ray background file to have the same exposure time as the stowed background). This part-synthetic background provides a very good match to the spectra extracted from the edge of detector and accounts for the particle background in the centre of the observation properly.

The advantage of this procedure over modelling the soft component in each spectral fit, is that we can easily account for detector variation (bad pixels, vignetting, etc) and that it simplifies the spectral fitting by only having one background dataset per observation.

2.2 Radio observations

VLA observations of the radio source, J1632+0534 at the centre of A2204, were performed on 2007 July 3 at 0.329 GHz in the ‘‘A’’ configuration, and on 2007 November 25 at 1.4 GHz in the ‘‘B’’ configuration. We also make use of data from the VLA archive at 1.4, 5 and 8.4 GHz. Details regarding the radio observations are summarised in Table 2. All data were reduced in AIPS (Astronomical Image Processing System) following the standard procedures. Absolute flux density calibration was tied to observations of 3C286.

3 IMAGING

3.1 Central structure

In Fig. 1 (left panel) we show a merged exposure-corrected image of the core of the cluster. As previously described in Sanders et al. (2005), there is a core with flat surface brightness of dimensions of 7×9 arcsec. This core is embedded within another flat central ‘‘plateau’’ of radius ~ 10 arcsec. A plume-like feature extends from the west of the plateau, wrapping around from south to east.

The unsharp masked images in Fig. 1 (centre and right panels) show there is considerable structure visible inside the inner 6 arcsec radius, and the surrounding plume.

The central radio nucleus (J1632+0534) corresponds with a peak in the X-ray emission offset to the north of the centroid of the cluster (Fig. 2). The X-ray spectrum is compatible with a $\Gamma = 2.0 \pm 0.2$ powerlaw with a luminosity of $(1.4 \pm 0.3) \times 10^{42}$ erg s $^{-1}$. The nuclear spectrum is equally well fit with a thermal model with a best fitting temperature suspiciously close to that of the surrounding gas ($kT \sim 3$ keV).

Although noted in a few surveys, the radio source at the centre of the Abell 2204 cluster, TXS1630+056 = 1632+0534, has received little attention. This is understandable given its relatively modest flux and small angular size compared to most radio galaxies in cooling core clusters.

At 8.4 GHz J1632+0534 consists of a compact nucleus with flux density 16.7 mJy with weaker compact components to the north and south. The total flux density is ~ 22 mJy. The nucleus has a flat spectrum. Components on either side of the nucleus are steep spectrum, with some evidence for extended, steep spectrum emission at 1.4 GHz with a largest angular size of 15 arcsec (39 kpc). A steep-spectrum component, with flux density ~ 1 mJy is present about 10 arcsec N of the nucleus. This component is likely associated with the nearby companion galaxy seen in Fig. 2. At 1.4 GHz J1632+0534 also extends to the south-west, and there is a hint of diffuse emission 10 arcsec to the east and west that reaches 5 times the rms noise level of 30 microJy/beam and could possibly be associated with a mini-halo (Fig. 2). The total flux density of J1632+0534 at 1.4 GHz is 58 mJy, and the corresponding total radio power at 1.4 GHz is 3.7×10^{31} erg s $^{-1}$ Hz $^{-1}$. Our 0.33 GHz (90 cm) image, with noise level 1 mJy beam $^{-1}$, does not reveal any further extension, any old emission from a previous outburst, or any sign of a mini-halo or cluster halo.

The X-ray and radio nuclei are coincident with the optical nucleus of one of the central galaxies. The two central galaxies are likely to be associated because of the small velocity difference along the line of sight (Jenner 1974).

The plateau contains a number of X-ray surface brightness depressions. These include ones to the east, west, south-east and north-east. There are also possible depressions to the south and north. Each of the depressions has a radius of around 1.5 arcsec (3.9 kpc), although the western hole could be larger with a radius of around 2 arcsec (5.2 kpc). There is also the depression at the X-ray centroid of the core and plateau, with a radius of around 1.5 arcsec. This depression lies around 2 arcsec south-east of the nucleus.

Such depressions are seen in the cores of galaxy clusters, where the relativistic gas in radio lobes displaces the thermal X-ray plasma (e.g. Hydra A, McNamara et al. 2000; Perseus, Böhringer et al. 1993, Fabian et al. 2000; Abell 2052, Blanton et al. 2001; Centaurus, Sanders & Fabian 2002). None of these depressions are coincident with sources in our new deep radio data, suggesting that if they are coincident with radio bubbles, the electrons in the bub-

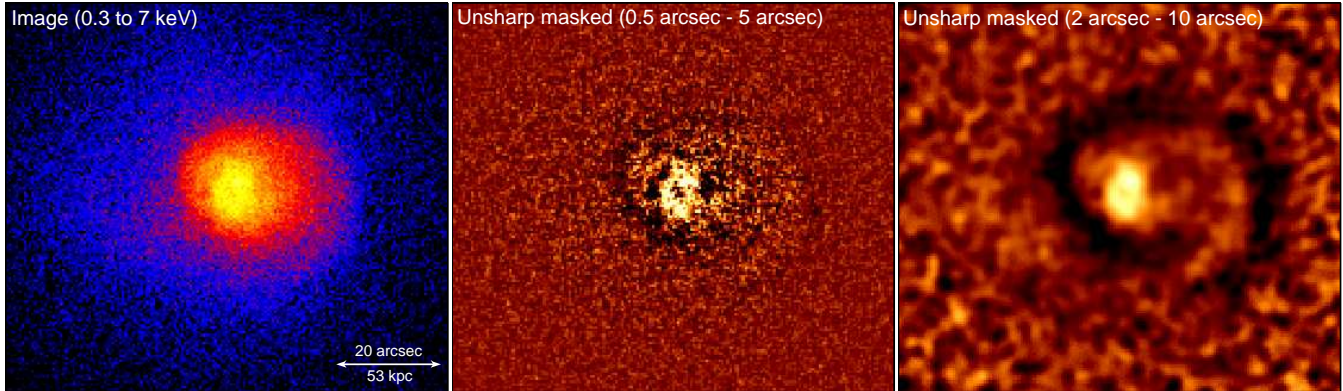


Figure 1. (Left panel) 0.3 to 7 keV image of the core the cluster with 0.492 arcsec pixels. (Centre panel) Unsharp-masked image, created by subtracting images smoothed by Gaussians of $\sigma = 0.5$ and 5 pixels (regions with more emission on small scales are shown as lighter here). (Right panel) Unsharp-masked image, created by subtracting images smoothed with $\sigma = 2$ and 10 arcsec.

Table 2. Radio observational parameters.

Source	Date	Frequency (MHz)	Bandwidth (MHz)	Config.	Duration (min)
J1632+0534	Jul 2007	322/329	6.25	A	171
	Nov 2007	1365/1435	50	B	83
	Apr 1998	1365/1435	25	A	240
	Apr 1998	4635/4885	50	A	61
	Aug 1998	8115/8485	50	B	134

bles have aged too much to be observable in radio (i.e. they are “ghost” cavities).

3.2 Outer structure

We show in Fig. 3 (left panel) the larger scale surface brightness in the 0.5 to 5 keV band (generated from the lower background ACIS-I observations). In this image we used the MAKE_READOUT_BG script (written by M. Markevitch) to generate out-of-time events background images to subtract from the data. Out-of-time events occur while the detector is being read, leading to a streak in the readout direction (the exposure of these events is effectively 1/78.05 of the normal exposure). Without subtraction, the streak runs about 12 degrees north from the west through the centre of the cluster for the 7940 observation (coincidentally running along the plume).

In Fig. 3 (right panel) we show the fractional deviation of each pixel in the surface brightness image from the average at that radius (accounting for the effects of background and out-of-time events). Immediately apparent are enhancements in roughly the east-west direction, and depressions in the north-south direction.

To examine these in more detail, Fig. 4 displays an azimuthal surface brightness profiles at two different radii, chosen to coincide with the inner (southern) and outer (northern) decrements. The decrements are very significant, at around the 30 per cent level.

The northern decrement and its surrounding bright rims can easily be seen in an image of the cluster with a large binning factor applied (Fig. 5). In addition, an edge like feature is apparent 950 kpc to the north-west of the cluster, close to the maximum extent of the northern decrement. This edge is also just visible in Fig. 3. *XMM-Newton* MOS images of the cluster also show the

northern bubble, though its edge lies close to the edge of the central MOS detector.

The most important question is the physical nature of these decrements in Fig. 3 and Fig. 4. The first option is that they are an artefact of the analysis procedure. If the cluster has an elliptical surface brightness distribution on the sky, then if we subtract the average surface brightness at each radius we will obtain a sinusoidal profile. Numerical tests show that we need approximately a 2:1 ratio of major to minor axis to achieve the 30 per cent surface brightness variation observed. Fitting elliptical surface brightness models to the data imply that the cluster is fairly close to circular (see also Hashimoto et al. 2007 who find a low ellipticity), excluding the very inner regions. The profiles (Fig. 4) are also not very sinusoidal, particularly the sharp edges to the depression to the north. Fig. 5 shows that there are real surface brightness enhancements surrounding the northern decrement, indicating it is not a data analysis issue.

Therefore the depressions are likely to be real cluster features. Their morphology is similar to the X-ray cavities observed in other galaxy clusters. In this case the cavities are very large compared to those typically found: the northern cavity has a radius of around 85 arcsec (225 kpc) and the southern one 55 arcsec (145 kpc). If they are cavities, then they are significantly larger than the 100 kpc radius cavities in MS 0735+7421 (McNamara et al. 2005) and Hydra A (Wise et al. 2007). The cavity interpretation is favoured by the enhancement in surface brightness around the depression, particularly for the northern feature (see Fig. 5). These enhancements would correspond to the bright rims seen around bubbles in other objects.

Instead of a single episode, the depressions may be the cumulative result of a set of repeated outbursts along a single axis. These outbursts could accumulate into a large region occupied by non-

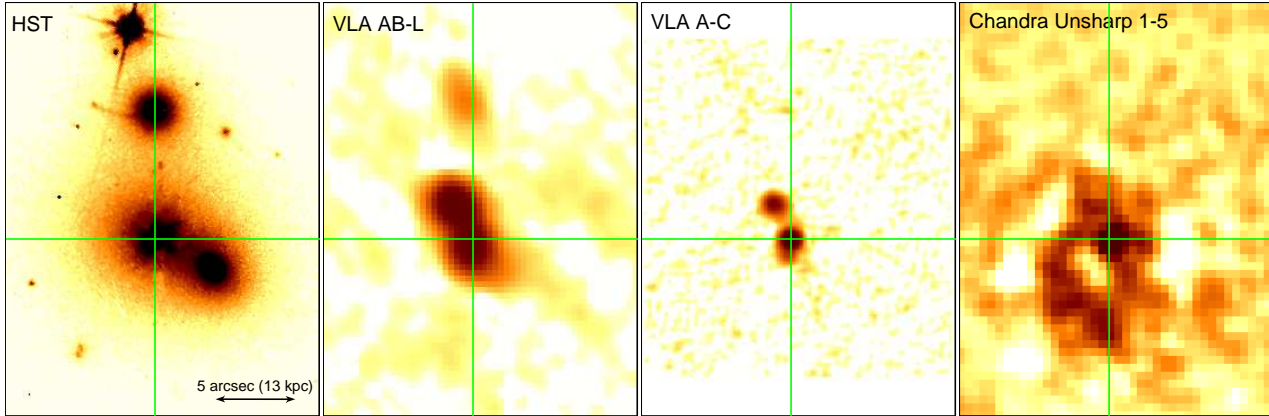


Figure 2. Comparison of *HST* image of the central galaxies, VLA L band (20 cm) image, VLA C band (6 cm) image and *Chandra* unsharp-masked image. The *HST* image was created by combining datasets U5A44101R and U5A44102R (F606W filter).

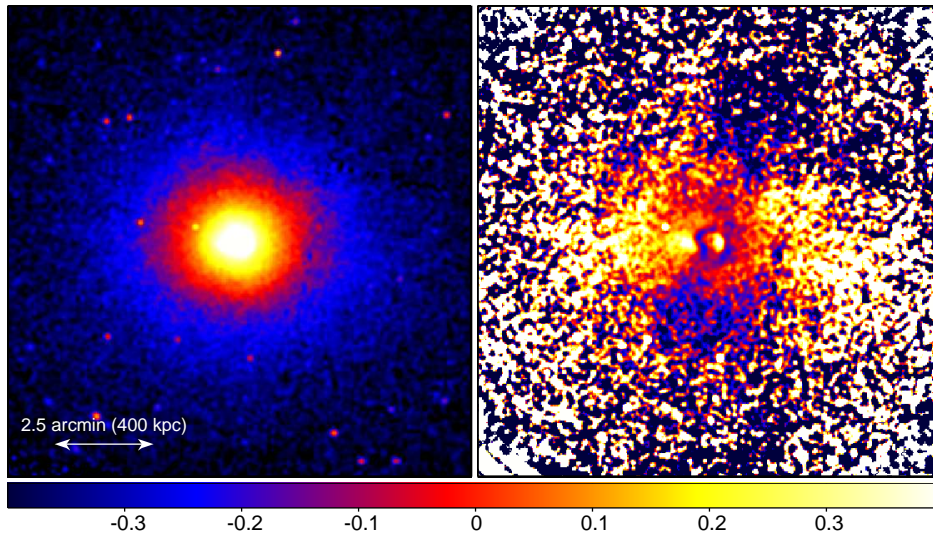


Figure 3. (Left) X-ray image of the larger scale cluster emission between 0.5 and 5 keV from the ACIS-I observations, binned into pixels of 2.0 arcsec and smoothed with a Gaussian with $\sigma = 6$ arcsec. (Right) Fractional difference of each pixel from the average at that radius. The image was then smoothed with a $\sigma = 6$ arcsec Gaussian. The colour bar shows the numerical scale of the fractional differences.

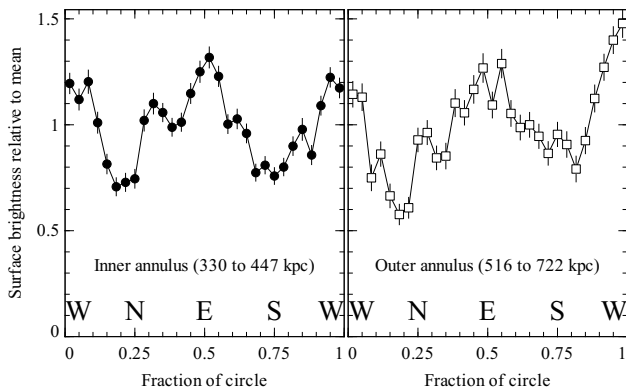


Figure 4. Surface brightness profile around in azimuth at two radii, chosen to overlap with the inner decrement to the south and outer decrement to the north. The profiles have been normalised by the average at each radius.

thermal particles, displacing the thermal plasma. Repeated sets of bubbles along one direction have been seen in Hydra A (Wise et al. 2007), estimated to have lasted over 200–500 Myr. In addition the Perseus cluster shows a low-thermal-pressure channel and further possible bubbles to the south beyond the outermost southern radio bubble. There is also a possible intact bubble 170 kpc to the north (Sanders & Fabian 2007).

Bubbles should “pancake” at large radius (Churazov et al. 2001), where the bubble density matches the ambient density. It may be that they have not yet done so here, perhaps because of magnetic fields.

Other possibilities include a merger. However, the cavities with their sharp edges appear unlikely to be the result of a merger. Finally, we could perhaps be observing the accretion of matter onto the cluster along filaments to the east and west of the image. This could be a possibility as the temperature of the gas is enhanced along these directions (see Section 4.2). However the temperature enhancement can only be measured close to the centre of the cluster, not where the material would be being accreted. Also the sharp edges of the depressions make this explanation unlikely.

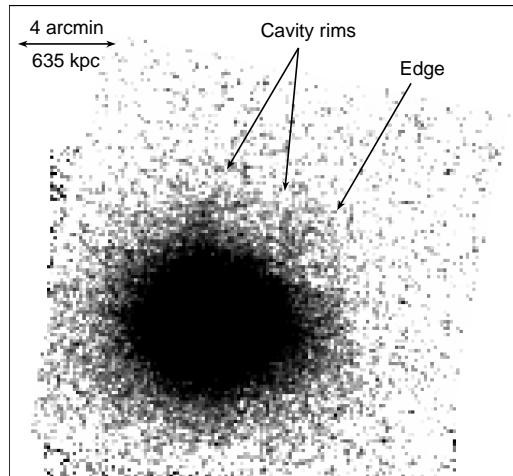


Figure 5. 0.5 to 5.0 keV exposure-corrected and background-subtracted image of the outer region of the cluster, with point sources excluded, binned using 7.87 arcsec pixels and smoothed with a Gaussian of 1 pixel.

4 SPECTRAL FITTING

4.1 Mapping the cluster core

To investigate the metallicity and temperature structure in the core of the cluster, we applied spatially resolved spectroscopy techniques. We divided the central $\sim 70 \times 70$ arcsec into bins using the Contour Binning algorithm (Sanders 2006) which follows surface brightness variations. We chose regions with a signal-to-noise ratio of 30 (around 900 counts), restricting the length of the bins to be at most two times their width.

We extracted spectra from each of the datasets, generating appropriate responses and ancillary responses. Background spectra were extracted from the part-synthetic backgrounds (Section 2.1). The 6104 and 7940 datasets were added together (as they use the same detector), weighting responses and backgrounds.

We fit each spectrum with an absorbed APEC model (Smith et al. 2001). The absorption was fixed to the Galactic value, but the temperature, metallicity and emission-measure were allowed to vary in the fit. The fitting procedure minimised the C-statistic (Cash 1979) and we fitted the data between 0.5 and 7 keV.

Shown in Fig. 6 are the derived temperature and metallicity maps of the core of the cluster, with an image of the cluster at the same scale. Note that the temperature is emission-weighted and projected and that the metallicity measurements are most sensitive to iron. The bright core and plateau corresponds to a cool region, where the projected temperature drops below 3 keV in some places. There also appears to be an extension in cool gas along the plume to the west of the core.

The metallicity structure appears to have a different morphology. The core and plateau contains a number of metallicity inhomogeneities. The most significant is a high metallicity region around 11 arcsec to the south of the centre (Fig. 7). This is adjacent to a region with low metallicity to the south-east of the core at the same radius. We show the combined spectrum in the three high metallicity bins compared to the three low metallicity bins to their east in Fig. 8. The metallicity of the low metallicity region is $0.38^{+0.17}_{-0.14} Z_{\odot}$ and the high metallicity region is $1.60^{+0.39}_{-0.32} Z_{\odot}$. If both regions are constrained to have the same temperature, this makes very little difference to this result. Markov Chain Monte Carlo (MCMC) tests in XSPEC confirm these uncertainties.

Looking at the spectra (Fig. 8), the significance of the enhancement in the three high metallicity bins relative to the three low metallicity bins is around 4σ (corresponding to a probability of 6×10^{-5} of occurring by chance). There are 168 bins in the image, so there are approximately 170 sets of three radial bins and around 340 unique sets of three radial bins next to three radial bins. This increases the chance probability to around 2 percent.

However, the highest, second highest and fifth highest metallicity bins are next to each other. They are statistically independent bins, so the chances of this occurring by chance are the order of $(2/167)(3 \times 2/164) \sim 4 \times 10^{-4}$. This small probability is decreased still further by the chances of finding three of the lowest metallicity regions in the central part of the cluster immediately adjacent to these high metallicity regions.

4.2 Mapping the outer regions of cluster

We show in Fig. 9 temperature and metallicity maps of a $\sim 870 \times 870$ kpc box around the cluster core. To generate these maps, we binned the image to have regions with a signal-to-noise ratio of 63 (~ 4000 counts) with the Contour Binning algorithm. We generated combined spectra from the 6104 and 7940 ACIS-I observations, fitting the data with the same APEC model as for the core region.

We investigated the effect of accounting for out-of-time events (events occurring while the CCDs are being read out), but this made little difference to the spectral fitting results for this region. Minimising χ^2 instead of the C-statistic made some difference, but the morphology remained very similar.

The temperature map shows that the temperature of the gas to the east flattens off to around 8 keV, until a radius of around 190 kpc, where it steeply rises to above 12 keV. The temperature rises more steeply to the west. At large radius there is an apparent decline in temperature.

The metallicity map shows structure, as we found previously (Sanders et al. 2005). We find that the metallicity drops outside of the core, but rises again to form a ring or spiral around the core at a radius of around 150 kpc. It is unclear whether this metallicity structure is connected to the spiral-like feature in the very central regions (Fig. 6 centre panel).

One particularly interesting metallicity feature is the region of high metallicity around 300 kpc to the north. There is no high metallicity material at this radius to the south. This can be demonstrated by examining the spectra directly of two diametrically opposite bins directly (Fig. 10; the bins examined are marked in Fig. 9). There is no evidence for Fe-K line emission for the southern spectrum, but it is seen strongly for the northern region.

The best fitting metallicities are zero for the southern region (the 2σ upper limit is $0.28 Z_{\odot}$). The metallicity of the northern region is 0.77 ± 0.21 . We have confirmed with the MCMC functionality in XSPEC that the difference in metallicity between the two regions is significant to 3σ .

4.3 Profiles of cluster properties

To examine the cluster properties as a function of radius, we extracted projected spectra from circular annuli chosen to give a reasonable quality spectrum. We only used the 7940 dataset here, as it simplified much of the analysis without much change in signal-to-noise ratio. Using the Direct Spectral Deprojection method of Sanders & Fabian (2007) (tested in Russell et al. 2008), we generated deprojected spectra from the projected spectra. We then fit-

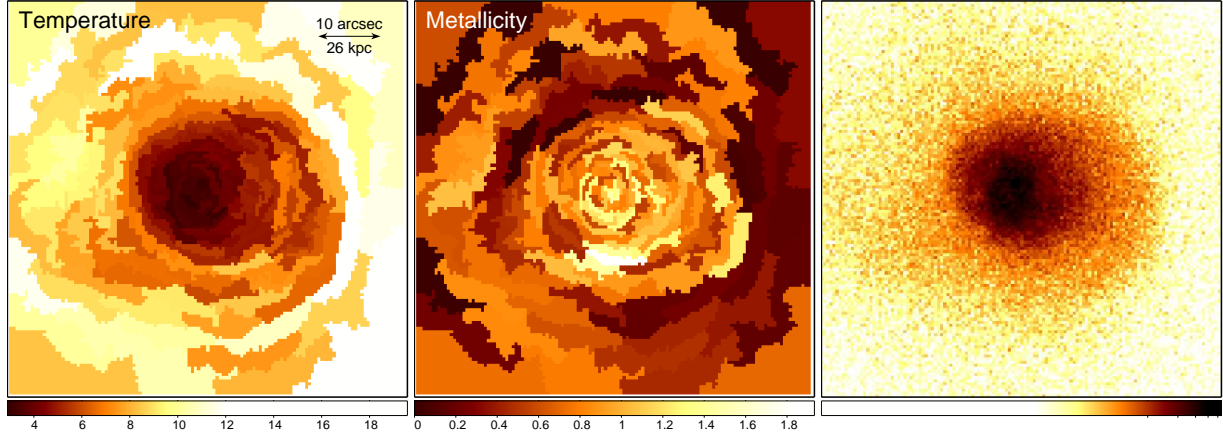


Figure 6. Temperature (left), metallicity (centre) and image (right) of the core of the cluster at the same spatial scale. The units of temperature are KeV and metallicity Z_{\odot} . These maps were created by fitting models to spectra with around 900 counts. 10 arcsec corresponds to a distance of ~ 26 kpc at this redshift. Uncertainties in temperature range from around 6 per cent in the centre to 30 per cent in the outer parts of this image. Metallicities are uncertain to around $0.35 Z_{\odot}$.

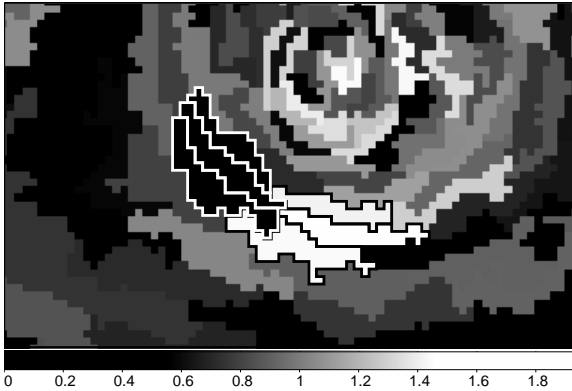


Figure 7. Zoom up of the metallicity map showing the three adjacent high metallicity regions (bordered in black) and the three adjacent low metallicity regions (bordered in white), examined in Section 4.1 and Fig. 8. The units are Z_{\odot} and each pixel is 0.49 arcsec (1.3 kpc) in size.

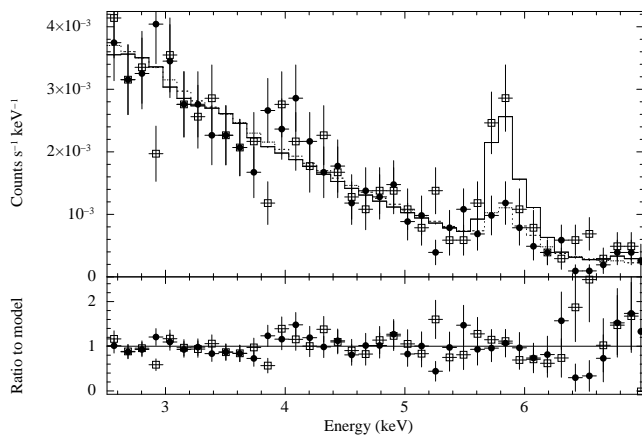


Figure 8. Comparison of the rebinned higher energy part of the spectrum between the high and low metallicity regions 11 arcsec to the south and south-east of the core (Fig. 6). The solid and dotted lines are the best fitting models. The bottom panel shows the ratio of the rebinned data to model.

ted single temperature APEC models to the projected and deprojected spectra to create temperature, metallicity and emission measure profiles. We included the effects of background and out-of-time events in this analysis, assumed Galactic absorption, grouped the spectra to have at least 25 counts per spectral bin, fitted the data between 0.5 and 7 keV and minimised the χ^2 to find the best fitting model.

Fig. 11 shows the projected and deprojected temperature and projected metallicity profiles out to a radius of ~ 1200 kpc. Beyond this radius there is little cluster emission in the spectra. The plot also shows the electron density, calculated from the emission measure of the fit to the deprojected spectra. By multiplying the deprojected electron density and temperature, we calculated the pressure. We also computed the entropy using $S = kTn_e^{-2/3}$. To calculate the errors on the pressure and entropy, we assumed that the errors on temperature and density were independent. Most of the uncertainty is in the temperature, so this assumption could be made.

We are able to measure a density variation of a factor of ~ 600 , pressure ~ 300 and entropy ~ 150 . We observe the temperature of the ICM to decline with radius beyond 400 kpc (in the projected spectra, which have smaller error bars). The temperature profile in the outskirts agrees reasonably well with the *Suzaku*, *Chandra* and *XMM-Newton* profiles published by Reiprich et al. (2008). In the centre, we find values similar to their *Chandra* results from a shorter observation. The peak *Chandra* temperatures are higher than *Suzaku* or *XMM* and the central temperature drops more steeply. This is probably due to PSF effects, though there are claims that the *Chandra* effective area calibrations contribute to the higher peak temperatures. Interestingly, our results show that the entropy profile remains flat beyond 550 kpc, similar to what was found in PKS 0745-191 (George et al. 2008). The entropy profile appears to break at 72, 240 and 650 kpc.

The maps suggest that there is structure in the properties of the cluster as a function of angle. We split up each annulus into four 90 degree sectors, pointing towards the north, east, south and west. Fig. 12 shows the projected and deprojected temperature profiles for each of these sectors. Much of the structure in the temperature maps is seen in the profiles. For instance, 120 kpc to the west is a higher temperature region. At larger radius to the west, where there

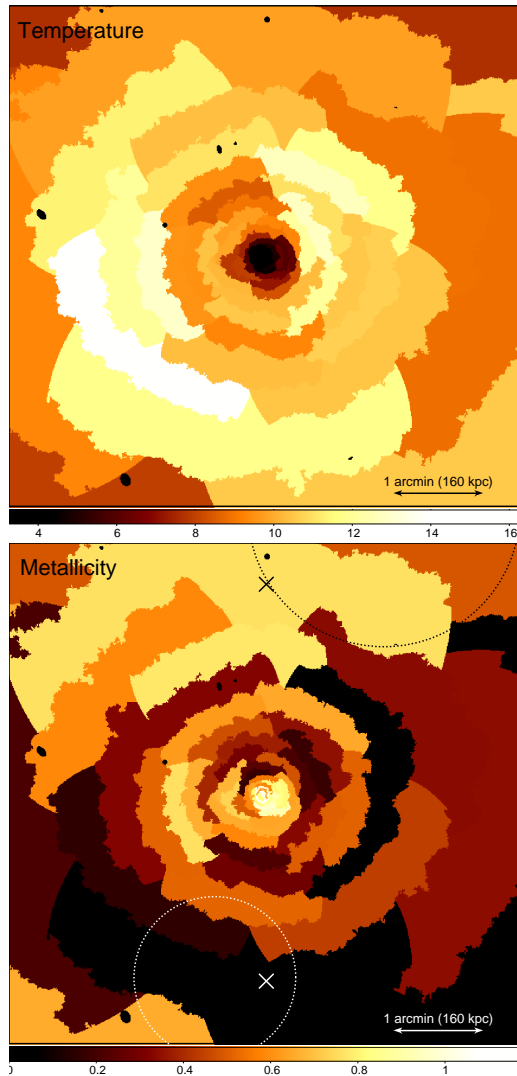


Figure 9. Larger scale temperature (top; in keV) and metallicity (bottom; in Solar units) structure, created by fitting spectra with a signal-to-noise ratio of greater than 63. The two regions marked with an “X” are examined spectrally in Fig. 10. The outer surface brightness depressions are marked as dotted circles on the metallicity map.

is brighter cluster emission than to the north or south (Fig. 5), the gas is cooler than in the other sectors.

The projected metallicity profiles in the quadrants (Fig. 13) show interesting variation. We see the high metallicity ring strongly to the south at a radius of around 240 kpc. We also see the large metallicities to the north 650 kpc from the nucleus.

In Fig. 14 (top panel) are plotted the deprojected densities in the four sectors. In the bottom panel we display the fractional difference of each density from the average at that radius. The plot shows the lower density regions to the north (beyond 300 kpc) and south (around 250 kpc) corresponding to the depressions in the surface brightness image.

4.4 Cool gas in the core

To examine the amount of cool gas which could be present in the core of the cluster, we extracted the spectrum from the in-

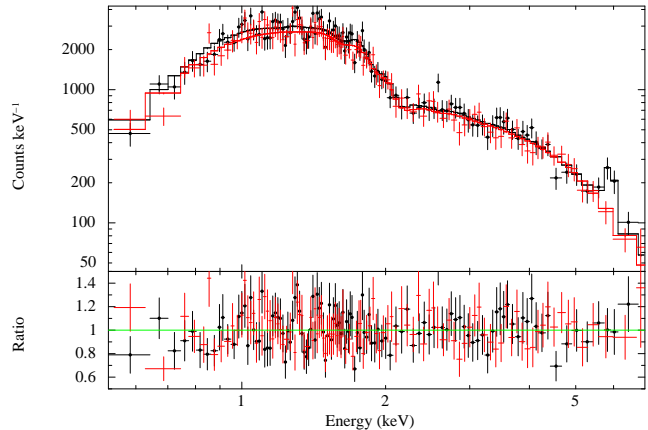


Figure 10. Comparison of the spectra from regions around 350 kpc to the north (circles) and south (no circles). The solid lines in the top panel are the best fitting spectral models. In the bottom panel is shown the ratio of the data to the best fitting spectral model. The data have been rebinned.

Table 3. *XMM-Newton* RGS datasets analysed. Exposures given are for the RGS1 instrument.

Observation ID	Date	Exposure (ks)
0112230301	2001-09-12	21.4
0306490101	2006-02-06	23.4
0306490201	2006-02-08	23.5
0306490301	2006-02-12	23.1
0306490401	2006-02-14	22.8

ner 100 arcsec radius. We fit a cooling flow model, made up of APEC+MKCFLOW components to account for the cluster and cooling emission. The MKCFLOW cooling flow model was computed with APEC spectra. Galactic absorption was assumed in the spectral fitting. The upper temperature and metallicity of the cooling flow model was tied to the APEC component and the lower temperature was fixed to 0.0808 keV (the lowest possible). The *Chandra* spectra were consistent with a $65 \pm 21 M_{\odot} \text{ yr}^{-1}$ mass deposition rate.

Much better determinations of the amount of cool gas can be made with high spectral resolution *XMM-Newton* RGS data (see Peterson & Fabian 2006 and references therein). We processed each of the RGS observations of Abell 2204 (Table 3) with SAS version 8.0.0. We used a PSF extraction region of 90 per cent and a pulse-height distribution region of 95 per cent. We created combined first-order RGS1 and combined RGS2 spectra and responses using the RGSCOMBINE task. The data were grouped to have at least 25 counts per spectral bin. Background model spectra were created with RGSBKGMODEL.

We fit the first-order data between 7 and 26 Å with a multi-temperature model. The temperature components were VAPEC models with fixed temperatures of 0.25, 0.5, 1, 2, 4 and 8 keV but free normalizations. The components shared the same metallicities, with O, Ne, Mg, Si, Fe and Ni free in the fits, and with S, Ar and Ca tied to Fe. The components were absorbed with fixed Galactic absorption. We did not account for the spatial distribution of the source in the modelling as the bright region is small compared to the *XMM* PSF. We fit the model to minimize the χ^2 statistic. The reduced χ^2 of the best fitting model was $0.994 = 1273.56/1281$.

In Fig. 15 we show the best fitting emission measures for each of the temperature components (these are the normalizations pro-

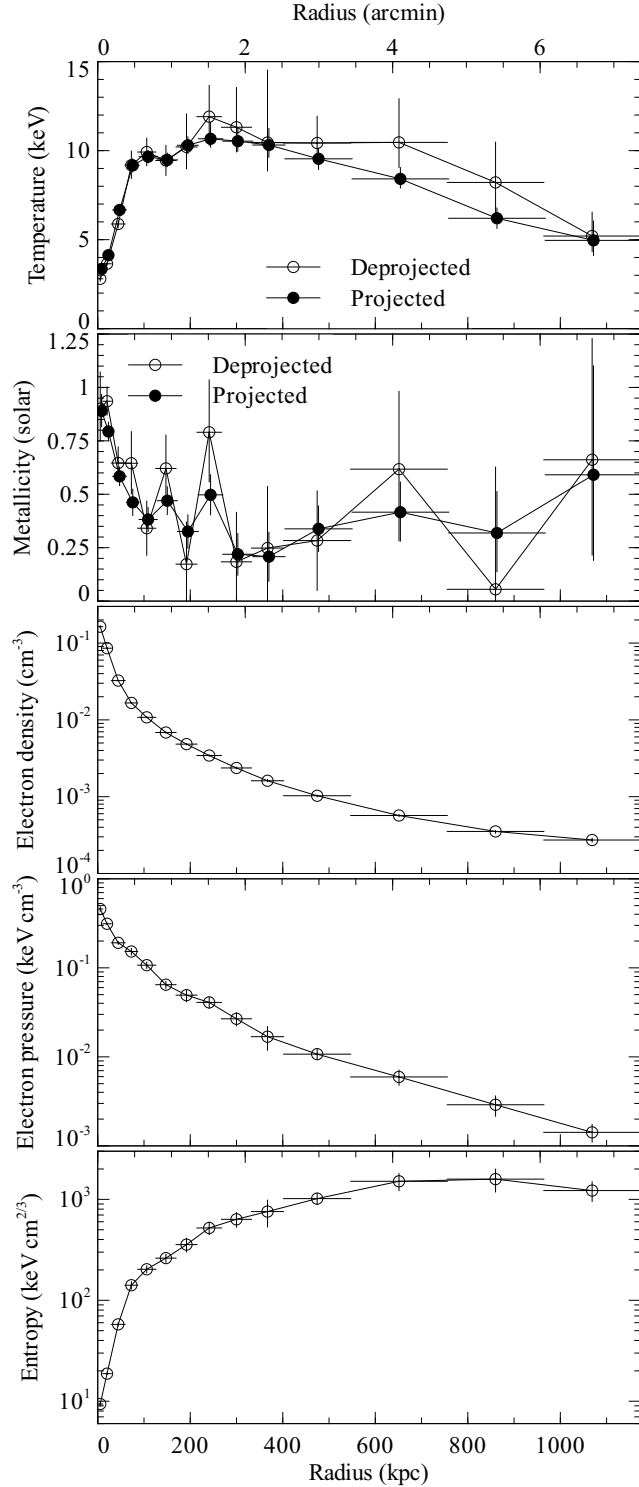


Figure 11. Temperature, metallicity and electron density profiles for the outer regions of the cluster. Also shown are the computed electron pressure and entropy profiles.

duced by XSPEC). Also plotted are the emission measures found by fitting a simulated spectrum of a cooling flow with a mass deposition rate of $200 M_{\odot} \text{ yr}^{-1}$ cooling from 8 to 0.0808 keV. We also plot the normalizations for a $65 M_{\odot} \text{ yr}^{-1}$ cooling flow, as found from the *Chandra* spectra.

We show in Fig. 16 the fluxed version of the spectrum. There

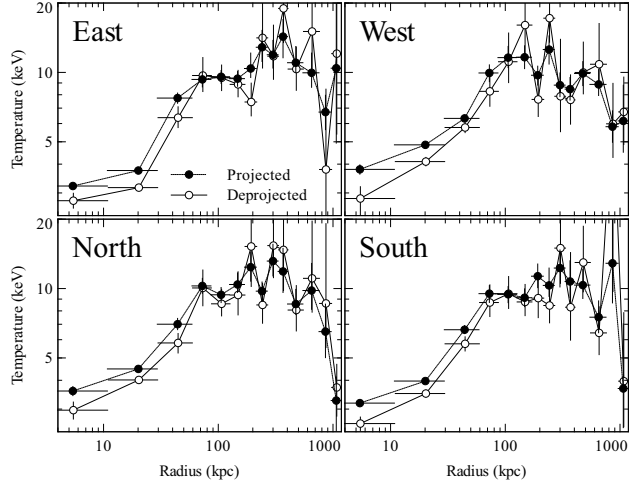


Figure 12. Projected and deprojected temperature profiles in four sectors.

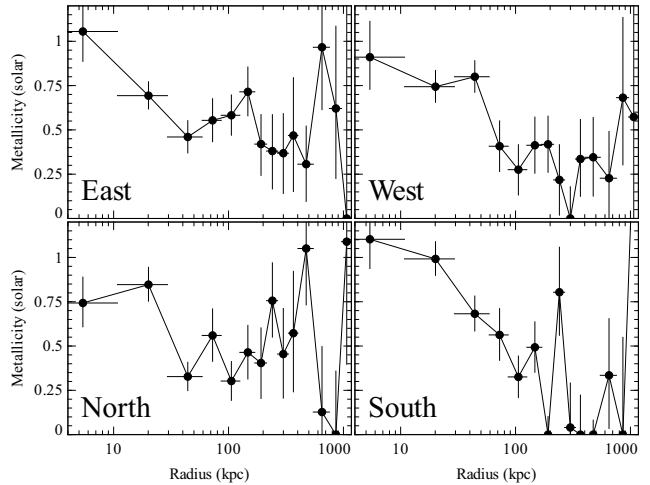


Figure 13. Projected metallicity profiles in four sectors.

are hints of the two strongest Fe XVII emission lines. Fitting zero-width Gaussian Fe XVII lines to the raw spectrum, and using an F-test to test for the significance of the line components gives a chance probability of 1.5×10^{-3} (3.2σ) for the redshifted 17.06 Å line, but only a chance probability of 0.33 (1σ) for the redshifted 15.01 Å line. The 17.06 Å line has a luminosity of $(7.6 \pm 2.6) \times 10^{41} \text{ erg s}^{-1}$ (which is compatible with a $120 M_{\odot} \text{ yr}^{-1}$ cooling flow)..

Fitting the RGS data with a model made up of a thermal VAPEC component and a VMCFLOW component cooling to 0.0808 keV gives a mass deposition rate of $124 \pm 25 M_{\odot} \text{ yr}^{-1}$ (fixing the upper temperature of the cooling flow to the VAPEC and using the same free metallicities as above).

5 DISCUSSION

5.1 Inner surface brightness depressions

The core of the cluster contains at least 5 or 7 X-ray surface brightness depressions. If these are interpreted as X-ray cavities caused by bubbles of relativistic plasma, then their *PV* energies are of the

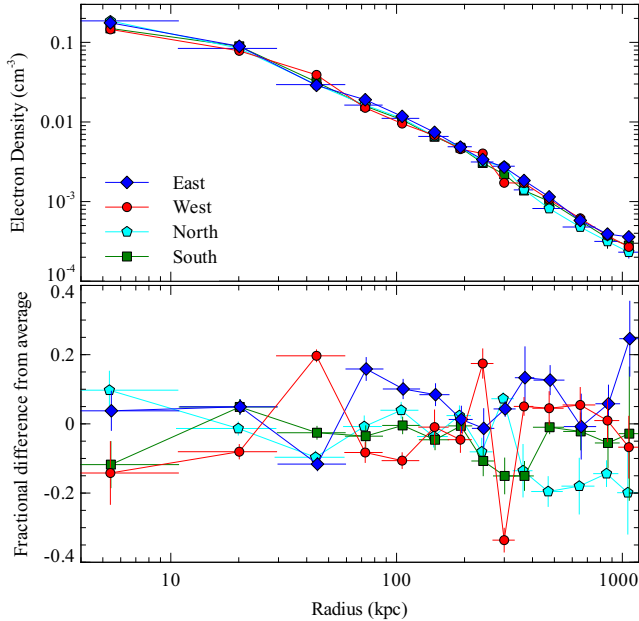


Figure 14. Deprojected electron density profiles in four sectors. The bottom panel shows the fractional difference of each profile to the weighted mean at each radius.

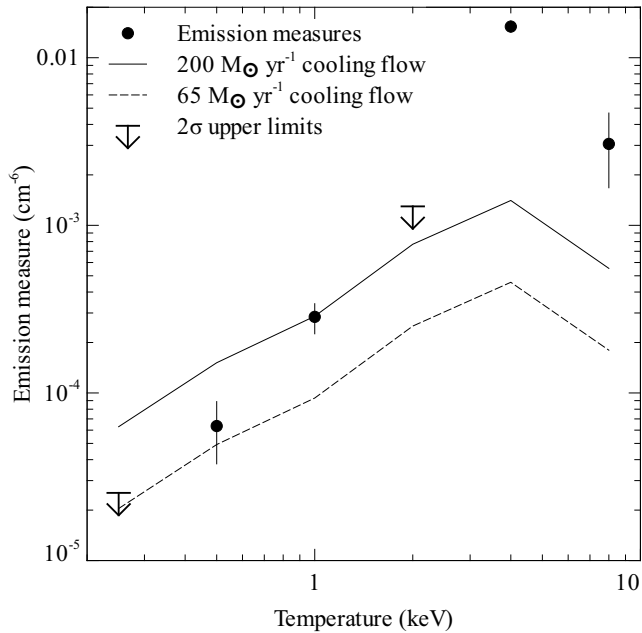


Figure 15. Best fitting emission measures for each of the components in the spectral fit to the RGS data.

order of 8×10^{57} erg (or a few times more for the larger depression), where P is the pressure of the surrounding ICM and V is the bubble volume. These are fairly typical values for cavities in clusters (Dunn & Fabian 2004). At the moderate distance of this cluster, the depressions are hard to spatially resolve. We observe no radio emission associated with the depressions, so we cannot confirm them as radio bubbles. If they are radio cavities they are ghost bubbles where the electrons have aged out of the observed band.

Their morphology is rather unusual for a radio bubble, how-

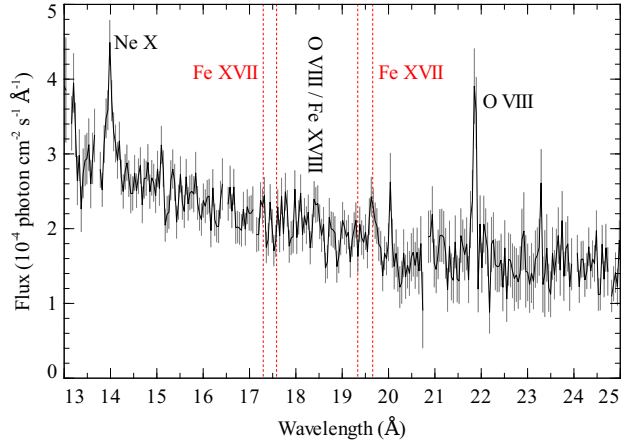


Figure 16. Fluxed and combined RGS spectra. This was fluxed using the RGSFLUXER tool with 850 wavelength bins. Note that the spectral fitting was applied to the raw spectra, not this fluxed spectrum. The vertical dotted lines show the expected position of the Fe XVII lines. The outer two lines should be the strongest ones.

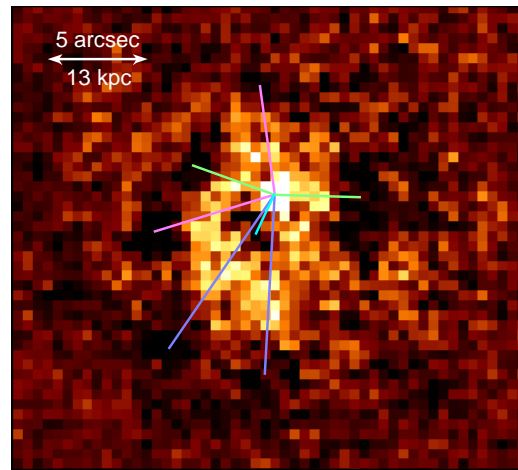


Figure 17. Unsharp-masked image of the very centre of the cluster, with lines connecting the radio/X-ray nucleus with the depressions in surface brightness. The image was created by subtracting the surface brightness image smoothed by Gaussians of $\sigma = 0.5$ and 5 pixels.

ever. There are 5 strong depressions, plus another two possible ones. They all lie roughly around 20 kpc distance from the X-ray centroid. However, if you measure the distance from the X-ray nucleus (Fig. 17), the north-east and west depressions at similar radius (~ 12 kpc), so are the north and east features (~ 16 kpc), and the south and south-east regions (~ 25 kpc), leaving the central depression at 6 kpc distance. This may be coincidental, but it fits with the picture of the bubbles being created in in pairs (except for the central depression). We do not know the component of distance from nucleus along the line of sight, however. It could be that these are bubbles like the series of ‘frothy’ bubbles in M87 (Forman et al. 2007).

Using a radius of 25 kpc (the maximum) and the sound speed implies a timescale of 2.7×10^7 yr. Using $4PV$ enthalpy (if the gas in the bubbles is relativistic; Bîrzan et al. 2004; Dunn & Fabian 2004), this would translate into a mechanical heating rate of 4×10^{43} erg s^{-1} per bubble.

The bolometric luminosity from the inner 100 kpc is $1.6 \times 10^{45} \text{ erg s}^{-1}$. 5 bubbles would fall short of providing the required heating rate to compensate cooling by an order of magnitude.

From the cavity heating power correlation of Bîrzan et al. (2008), the 1.4 GHz radio luminosity implies a cavity heating power of around $10^{44} \text{ erg s}^{-1}$. This power is similar to the calculated heating power of the cavities. It still falls short of the required heating power to prevent cooling by an order of magnitude. However, there are a couple of orders of magnitude scatter in the correlation between radio and heating power, so this is not at all conclusive.

We note that projection of cool gas in front of bubbles could create the complex morphology observed. The bright emission to the east of the bubbles in Perseus (Fabian et al. 2000) is much stronger than the deficit in the bubbles. If the bubbles were observed along a different line of sight they may be completely obscured or difficult to interpret. Therefore there may be much larger bubbles present in Abell 2204 than we infer. We would require a bubble around the same size as the bright central core to completely prevent cooling.

5.2 Outer surface brightness depressions

The cluster contains a surface brightness depression to the north, between radii of 135 and 295 arcsec (355 to 780 kpc). To the south, there is a depression between radii of 65 and 185 arcsec (170 to 490 kpc). Given their morphology, they are either old radio bubbles or the cumulative result of many generations of radio bubble.

We can estimate how much energy each cavity could inject mechanically into its surroundings as the enthalpy $4PV$. The average electron pressure (Fig. 11) can be fitted outside 200 kpc radius by a model with the form $P_e = 0.156[1 + (r/149.5 \text{ kpc})^2]^{-1.13} \text{ keV cm}^{-3}$. If the total thermal pressure at each radius is integrated over the volume of each bubble (assuming that they are spherical), this leads to enthalpies for the northern and southern cavities, respectively, of 9.9×10^{61} and $1.3 \times 10^{62} \text{ erg}$ (simply using $4PV$ with the pressure at the midpoint gives a very similar result). The total enthalpy is therefore around $2 \times 10^{62} \text{ erg}$.

If they are a single set of bubbles, to estimate their mechanical heating power, we need an appropriate timescale for the heating. If the bubble is rising at a terminal velocity (Churazov et al. 2001), then the timescale for it to rise to its current radius is $t_{\text{buoy}} \sim R\sqrt{SC}/2gV$ (Bîrzan et al. 2004; Dunn & Fabian 2004), where S is the cross-sectional area of the bubble, V is its volume, R is the distance of the bubble from the cluster nucleus, g is gravitational acceleration there and C is a drag coefficient, 0.75.

For the northern bubble, at a radius of 220 arcsec in the cluster, the mass enclosed is around $4.5 \times 10^{14} M_{\odot}$ (Clowe & Schneider 2002), which with our assumed value of H_0 , implies $g \sim 1.9 \times 10^{-8} \text{ cm s}^{-2}$. This leads to a buoyancy timescale of $2.7 \times 10^8 \text{ yr}$. The enclosed mass at the radius of the southern bubble is 2.6×10^{14} , implying the buoyancy timescale is $1.2 \times 10^8 \text{ yr}$. The total mechanical power of the two bubbles is around $5 \times 10^{46} \text{ erg s}^{-1}$. This value is larger still than the most powerful outburst known, MS 0735+7421.

If these cavities are produced by a single episode, then it must have avoiding heating the core of the cluster. We measure a minimum central mean radiative cooling time of $2.5 \times 10^8 \text{ yr}$.

If, however, the features are caused by the cumulative effect of many generations of radio bubbles then we can estimate how long the enthalpy would combat cooling in the cluster. The bolometric X-ray luminosity within 500 kpc is calculated from our spectral

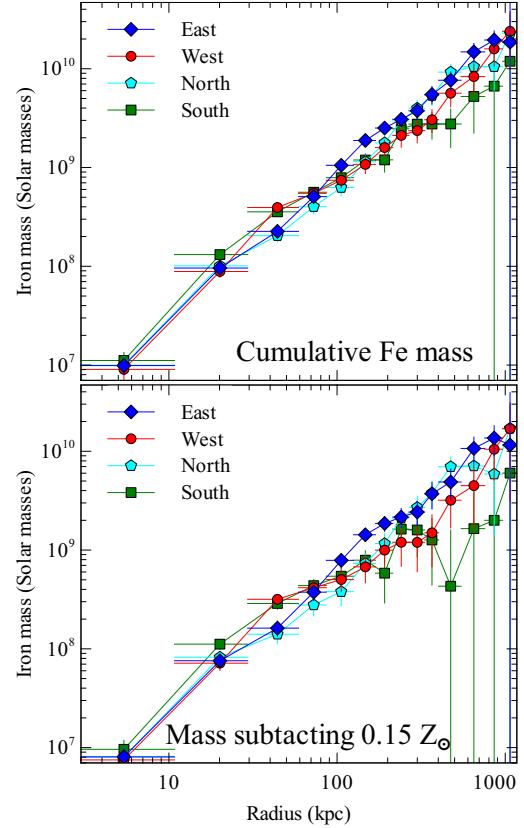


Figure 18. Cumulative iron mass profiles in the four different quadrants. The top panel shows the total Fe mass. The second shows the mass above a metallicity value of $0.15 Z_{\odot}$. The uncertainties were calculated using a Monte Carlo technique.

fitting results (Fig. 11) to be $3.5 \times 10^{45} \text{ erg s}^{-1}$. This means that the two features contain enough energy to stop cooling for around 2 Gyr.

5.3 Metallicity substructure

Abell 2204 presents metallicity substructure from the innermost regions (Fig. 6 left panel) to several hundred kpc radius (Fig. 9 bottom panel).

The metallicity substructure in the centre does not have any obvious correlation with the observed X-ray cavities. Bubbles are expected to drag cool, metal rich gas behind them (Churazov et al. 2001). However, when looking at the best data the picture is complex (Sanders et al. 2004; Sanders & Fabian 2007), with some high metallicity regions correlated with some bubbles. The metallicity structure on small scales points towards the intracluster medium not being well mixed (Sanders & Fabian 2002; Sanders et al. 2004, 2005; Durret et al. 2005; O’Sullivan et al. 2005; Fabian et al. 2005; Finoguenov et al. 2006; Sanders & Fabian 2007; Simionescu et al. 2008).

The high metallicity blob in the central region (Fig. 6 centre panel; Fig. 8) has a metallicity $1.2 Z_{\odot}$ greater than the neighbouring low metallicity region (or four times its value). Using a volume of $24 \times 12 \times 12 \text{ kpc}$ and an electron density of 0.1 cm^{-3} , this represents an enhancement of iron of $2 \times 10^7 M_{\odot}$.

To examine the outer northern metal enhancement, we calculated cumulative mass profiles in the four different quadrants,

shown in Fig. 18 (also shown is the iron mass profile above a metallicity value of 0.15, see Böhringer et al. 2004). These results assume the deprojected densities of Fig. 14 and projected metallicities of Fig. 13. The uncertainties were calculated by using a Monte Carlo calculation. Metallicity profiles were simulated from the original profiles and measurement errors (allowing them to be negative, using the larger side of the error bar and assuming a Gaussian distribution). Cumulative mass profiles were calculated from each simulated metallicity profile. The median, 16th and 84th percentiles were calculated to obtain the final cumulative mass and uncertainties. The plot shows there is an excess of a few times $10^9 M_{\odot}$ of iron towards the north and east compared to the south (the east is enhanced in mass compared to the north as the density is higher there as is no surface brightness depression). We note that metal masses can depend on the inhomogeneity of the metallicity distribution (Kapferer et al. 2007).

The northern outer metal enhancement may be associated with the cavity to the north, as the high metallicity region is roughly at the base of the northern cavity (Fig. 9). The data quality is not good enough to map this exactly. An outburst, a merger, or the cumulative effect of many radio bubbles may be required to lift the few times $10^9 M_{\odot}$ of iron from the cluster core to the outskirts. The metals could have been pulled out of the cluster core in the wake of a rising bubble or many bubbles. In addition the progress of the bubble(s) may have disturbed the cluster core enough to make the inner metallicity spiral, though smaller outbursts may have been responsible for this.

We note that the injection of metals into the intracluster medium should be a smooth process. The Type Ia supernovae in the central galaxy should be mainly responsible for the enrichment and these will be uniformly distributed over the galaxy. Some other process must be responsible for making the metallicity clumpy.

5.4 Diffusion coefficient

Given we have a high metallicity feature of the order of 6 kpc in size and if we assume it lasts for $\sim 10^9$ yr, this gives a diffusion coefficient of $< 10^{28} \text{ cm}^2 \text{ s}^{-1}$. This is similar to the value obtained for Centaurus (Graham et al. 2006) and an order of magnitude smaller than Perseus (Rebusco et al. 2005). Multiplying the sound speed and the 6 kpc scale gives a diffusion coefficient around $10^{30} \text{ cm}^2 \text{ s}^{-1}$. Unless these metallicity features are very short lived, then diffusion must be heavily suppressed, implying turbulent motions are damped on these scales.

5.5 Cool gas

The mass deposition rate calculated assuming that the X-ray luminosity comes from cooling alone and is in steady state is around $850 M_{\odot} \text{ yr}^{-1}$ (Peres et al. 1998). The RGS spectra from the cluster show evidence for cool gas down to around 0.5 keV from spectral fitting, and directly from the presence of the Fe XVII line. The quantity of cool gas is consistent with a cooling flow of $65 M_{\odot} \text{ yr}^{-1}$ down to the lowest detectable temperature. There is a wide range of temperature of the X-ray emitting material in cluster from around 12 keV all the way down to 0.5 keV. The gas below this temperature is consistent to 2σ with $65 M_{\odot} \text{ yr}^{-1}$.

This level of cooling is also consistent with the star formation rate of $14.7 M_{\odot} \text{ yr}^{-1}$ measured from infrared emission (O’Dea et al. 2008). We note that the optical spectra of Crawford et al. (1999) indicate only a rate of $1.29 M_{\odot} \text{ yr}^{-1}$. Feedback must be af-

fecting the gas below 0.5 keV to prevent at least 80 percent of it cooling.

6 CONCLUSIONS

We observe large and significant surface brightness depressions 570 and 330 kpc from the core of the cluster of galaxies Abell 2204. Morphologically they look like much larger versions of the X-ray cavities seen in the cores of galaxy clusters, but energetically they would be extremely powerful sources of mechanical heating if that were the case ($5 \times 10^{46} \text{ erg s}^{-1}$). They could, instead, be the accumulation of multiple episodes of radio bubble formation in the cluster core. The bubbles could rise in the same direction, forming a bubble repository at large radius. If this is the case they would have had to have avoided pancaking. The energy in this case could have offset cooling in the cluster over 2 Gyr. The core of the cluster contains several cavities, showing evidence for continued AGN feedback.

We see a high degree of metallicity substructure in the intracluster medium, from a 12 kpc feature containing $10^7 M_{\odot}$ of iron in the core, to a massive feature with $10^9 M_{\odot}$ of iron at 400 kpc radius to the north. These results, with other observations of the intracluster medium, indicate that metals in the intracluster medium are not efficiently mixed. The northern metallicity feature could have been lifted by the giant outburst in the past, or the continuous action of smaller outbursts.

In the core of the cluster are small depressions which may be cavities generated by the nucleus. They could not provide enough heating to prevent cooling in the central region, however. There is evidence for cool X-ray emitting gas a factor of more than 10 lower in temperature than the outer parts of the cluster. A cooling flow of around $65 M_{\odot} \text{ yr}^{-1}$ could be operating, in the absence of heating.

In the future, upcoming bolometers and other high energy resolution detectors will allow us to gain a much better understanding of the dynamical state of the ICM. We will be able to see the direct effect of bubbles on the motion of the intracluster medium (although filaments allow us to observe this indirectly, see Fabian et al. 2003) and examine the turbulence on different scales.

ACKNOWLEDGEMENTS

ACF thanks the Royal Society for support. GBT acknowledges support for this work from the National Aeronautics and Space Administration through Chandra Award Number GO7-8124X issued by the Chandra X-ray Observatory Center, which is operated by the Smithsonian Astrophysical Observatory for an on behalf of the National Aeronautics and Space Administration under contract NAS8-03060.

REFERENCES

- Anders E., Grevesse N., 1989, *Geochim. Cosmochim. Acta*, 53, 197
- Birzan L., McNamara B. R., Nulsen P. E. J., Carilli C. L., Wise M. W., 2008, *ApJ*, 686, 859
- Birzan L., Rafferty D. A., McNamara B. R., Wise M. W., Nulsen P. E. J., 2004, *ApJ*, 607, 800
- Blanton E. L., Sarazin C. L., McNamara B. R., Wise M. W., 2001, *ApJ*, 558, L15

- Böhringer H., Matsushita K., Churazov E., Finoguenov A., Ikebe Y., 2004, *A&A*, 416, L21
- Böhringer H., Voges W., Fabian A. C., Edge A. C., Neumann D. M., 1993, *MNRAS*, 264, L25
- Buote D. A., Tsai J. C., 1996, *ApJ*, 458, 27
- Cash W., 1979, *ApJ*, 228, 939
- Churazov E., Brüggen M., Kaiser C. R., Böhringer H., Forman W., 2001, *ApJ*, 554, 261
- Clowe D., Schneider P., 2002, *A&A*, 395, 385
- Crawford C. S., Allen S. W., Ebeling H., Edge A. C., Fabian A. C., 1999, *MNRAS*, 306, 857
- Dunn R. J. H., Fabian A. C., 2004, *MNRAS*, 355, 862
- Durret F., Lima Neto G. B., Forman W., 2005, *A&A*, 432, 809
- Edge A. C., Stewart G. C., Fabian A. C., Arnaud K. A., 1990, *MNRAS*, 245, 559
- Fabian A. C., Sanders J. S., Crawford C. S., Conselice C. J., Gallagher J. S., Wyse R. F. G., 2003, *MNRAS*, 344, L48
- Fabian A. C. et al., 2000, *MNRAS*, 318, L65
- Fabian A. C., Sanders J. S., Taylor G. B., Allen S. W., 2005, *MNRAS*, 360, L20
- Finoguenov A., Henriksen M. J., Miniati F., Briel U. G., Jones C., 2006, *ApJ*, 643, 790
- Forman W. et al., 2007, *ApJ*, 665, 1057
- George M. R., Fabian A. C., Sanders J. S., Young A. J., Russell H. R., 2008, *ArXiv e-prints*, arXiv:0807.1130
- Graham J., Fabian A. C., Sanders J. S., Morris R. G., 2006, *MNRAS*, 368, 1369
- Hashimoto Y., Böhringer H., Henry J. P., Hasinger G., Szokoly G., 2007, *A&A*, 467, 485
- Jenner D. C., 1974, *ApJ*, 191, 55
- Kalberla P. M. W., Burton W. B., Hartmann D., Arnal E. M., Bajaja E., Morras R., Pöppel W. G. L., 2005, *A&A*, 440, 775
- Kapferer W., Kronberger T., Weratschnig J., Schindler S., 2007, *A&A*, 472, 757
- McNamara B. R., Nulsen P. E. J., Wise M. W., Rafferty D. A., Carilli C., Sarazin C. L., Blanton E. L., 2005, *Nature*, 433, 45
- McNamara B. R. et al., 2000, *ApJ*, 534, L135
- O'Dea C. P. et al., 2008, *ApJ*, 681, 1035
- O'Sullivan E., Vrtilik J. M., Kempner J. C., 2005, *ApJ*, 624, L77
- Peres C. B., Fabian A. C., Edge A. C., Allen S. W., Johnstone R. M., White D. A., 1998, *MNRAS*, 298, 416
- Peterson J. R., Fabian A. C., 2006, *Phys. Rep.*, 427, 1
- Rebusco P., Churazov E., Böhringer H., Forman W., 2005, *MNRAS*, 359, 1041
- Reiprich T. H. et al., 2008, *ArXiv e-prints*, arXiv:0806.2920
- Russell H. R., Sanders J. S., Fabian A. C., 2008, *MNRAS*, in press
- Sanders J. S., 2006, *MNRAS*, 371, 829
- Sanders J. S., Fabian A. C., 2002, *MNRAS*, 331, 273
- Sanders J. S., Fabian A. C., 2007, *MNRAS*, 381, 1381
- Sanders J. S., Fabian A. C., Allen S. W., Schmidt R. W., 2004, *MNRAS*, 349, 952
- Sanders J. S., Fabian A. C., Dunn R. J. H., 2005, *MNRAS*, 360, 133
- Sanders J. S., Fabian A. C., Taylor G. B., 2005, *MNRAS*, 356, 1022
- Schuecker P., Böhringer H., Reiprich T. H., Feretti L., 2001, *A&A*, 378, 408
- Simionescu A., Werner N., Finoguenov A., Böhringer H., Brüggen M., 2008, *A&A*, 482, 97
- Smith R. K., Brickhouse N. S., Liedahl D. A., Raymond J. C., 2001, *ApJ*, 556, L91
- Wise M. W., McNamara B. R., Nulsen P. E. J., Houck J. C., David L. P., 2007, *ApJ*, 659, 1153